

See discussions, stats, and author profiles for this publication at: <https://www.researchgate.net/publication/272134839>

Superstructure of TiO₂ Crystalline Nanoparticles Yields Effective Conduction Pathways for Photogenerated Charges

ARTICLE *in* JOURNAL OF PHYSICAL CHEMISTRY LETTERS · JUNE 2012

Impact Factor: 7.46 · DOI: 10.1021/jz3005128

CITATIONS

38

READS

37

3 AUTHORS, INCLUDING:



Zhenfeng Bian

Shanghai Normal University

30 PUBLICATIONS 1,911 CITATIONS

SEE PROFILE

Superstructure of TiO₂ Crystalline Nanoparticles Yields Effective Conduction Pathways for Photogenerated Charges

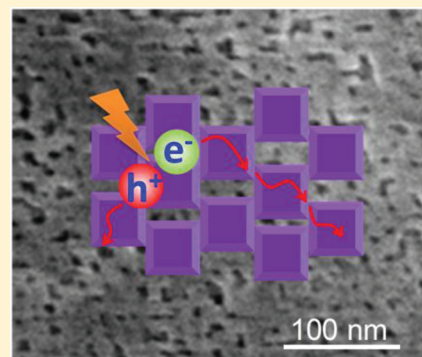
Zhenfeng Bian, Takashi Tachikawa,* and Tetsuro Majima*

The Institute of Scientific and Industrial Research (SANKEN), Osaka University, Mihogaoka 8-1, Ibaraki, Osaka 567-0047, Japan

S Supporting Information

ABSTRACT: Materials with intricate nanostructures display fascinating properties, which have inspired extensive research on the synthesis of materials with controlled structures. In this study, we investigated the properties of superstructures of TiO₂ to understand the inter-relationship between structural ordering and photocatalytic performance. The nanoplate anatase TiO₂ mesocrystals were chosen as the typical investigation objects, which were newly synthesized by a topotactic structural transformation. The TiO₂ mesocrystals displayed the superstructure of crystallographically ordered alignment of anatase TiO₂ nanocrystals with high surface area and large high-energy surface {001} planes exposed. The photoconductive atomic force microscopy and time-resolved diffuse reflectance spectroscopy were utilized to determine the charge transport properties of TiO₂ mesocrystals, and their features were highlighted by a comparison with reference TiO₂ samples, for example, anatase TiO₂ nanocrystals with similar surface area and single crystal structure. Consequently, it was found for the first time that such a superstructure of TiO₂ could largely enhance charge separation and had remarkably long-lived charges, thereby exhibiting greatly increased photoconductivity and photocatalytic activity.

SECTION: Energy Conversion and Storage; Energy and Charge Transport



As one of the most important semiconductors, TiO₂ is desirable in many applications that deal with environmental and energy problems. These applications include photodegradation of pollutants, water splitting, dye-sensitized solar cells, and lithium-ion batteries.^{1–3} The photocatalytic activity of TiO₂ is strongly dependent on the charge separation efficiency and specific surface areas. When TiO₂ is illuminated with UV light, electron–hole pairs are created simultaneously. Only a small part of photogenerated charge carriers spatially separate via diffusion and facilitate redox reactions to generate radical species on TiO₂ surfaces.^{1,2} If the charge recombination process is significantly retarded and a high specific surface area for adsorption of reagents is maintained, good photocatalytic activity will be obtained.

Self-assembled nanomaterials with highly ordered structures and controllable architectures have potentially tunable electronic, optical, and magnetic properties, which can be used in applications ranging from catalysis to optoelectronics.^{4–8} TiO₂ mesocrystals are oriented superstructures of TiO₂ nanocrystal building blocks and have recently emerged as a new class of porous TiO₂ materials.^{9–12} It is worth noting that anatase TiO₂ mesocrystals were first prepared by topotactic conversion from NH₄TiOF₃ mesocrystals.⁹ In addition, globular anatase TiO₂ mesocrystals with high surface areas were synthesized using the liquid phase method.^{10,11} Although these hydrothermal/solvothermal approaches have shown themselves to be advantageous in the synthesis of TiO₂ mesocrystals, they are complicated procedures, and hence, their large-scale applications are limited. Therefore, the development of a simple

pathway for the preparation of TiO₂ mesocrystals is of considerable interest.

More importantly, only a few studies have focused on the relationship between structures and properties of mesocrystals.¹³ For example, compared with bulk single crystals, the most common interpretation of the improved photocatalytic activity of mesocrystals is supported by the increase in the specific surface area. Furthermore, the open pores between nanocrystals allow the diffusion of the reactants and the penetration of light into the photocatalyst.¹² These improvements in performance are just some aspects of the mesocrystals. It has been proposed that the ordering of a nanocrystalline structure considerably influences charge transport and recombination, which are directly related to the performance of photocatalysts and photovoltaic cells.^{14–16} However, the relationship between the unique structural features and the properties of metal oxide mesocrystals as well as the ordered assemblies of metal oxide nanocrystals is still poorly understood.

We introduce here a facile, direct annealing approach for synthesizing nanoplate anatase TiO₂ mesocrystals with highly exposed {001} facets.¹⁷ Experiments on a single particle assembly revealed that the ordered superstructures produce a high yield of photogenerated charges and have high photoconductivity, which are difficult to achieve in traditional

Received: April 25, 2012

Accepted: May 10, 2012

Published: May 10, 2012

disordered systems consisting of crystalline nanoparticles, owing to the inevitable occurrence of charge recombination at the interface. Because of their superior properties, the TiO₂ mesocrystals developed in this study hold great promise for solar energy applications such as photocatalysis and photovoltaics.

During the one-step, template-free synthetic process, as illustrated in Figure 1, micrometer-sized plate-like TiO₂

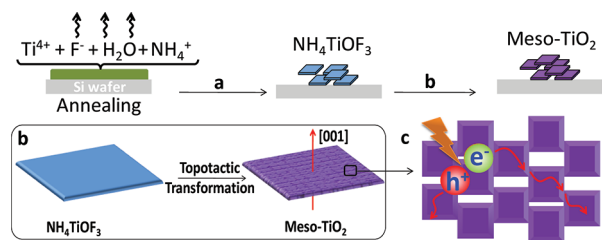


Figure 1. (a) The formation of NH₄TiO₃ at low annealing temperatures (250–300 °C). (b) The topotactic transformation from NH₄TiO₃ into Meso-TiO₂ at higher annealing temperatures (400–800 °C). (c) Porous Meso-TiO₂ consists of orderly aligned anatase nanocrystals with dominant {001} facets, leading to high efficiency of charge separation under UV light irradiation.

mesocrystal (Meso-TiO₂) was obtained after annealing a thin layer of aqueous solution containing TiF₄, NH₄F, and NH₄NO₃ covering a silicon wafer (see Supporting Information for details). In the annealing process, the material underwent changes in two stages. First, the precursors of Ti⁴⁺, F⁻, NH₄⁺, and H₂O began a series of combination reactions during evaporation of water at low annealing temperatures to form NH₄TiO₃ (Figure 1a). With further increase in annealing temperature, NH₄TiO₃ was easily transformed into TiO₂ (Figure 1b). When large amounts of nitrogen and fluorine were removed, the volume of nanoparticles decreased, and gaps or pores formed between nanoparticles, resulting in porous TiO₂ materials that consisted of anatase single-crystalline nanoparticles with dominant {001} facets. This well-ordered geometry should facilitate rapid and long-distance electron transport (Figure 1c).

The structure of Meso-TiO₂ annealed at 500 °C (Meso-TiO₂-500) was characterized by scanning electron microscopy (SEM) and transmission electron microscopy (TEM). Meso-TiO₂-500 shows a plate-like structure with a size of several micrometers (Figure 2a). It is composed of an ordered alignment of anatase TiO₂ nanocrystals with average diameter of around 39 nm (Figure 2b). Further, a porous structure with pore diameters of several nanometers is clearly observed and the pore size distribution is about 5 nm. The thickness of one representative plate TiO₂ crystal is about 80 nm, with a distribution between 50 and 300 nm (Figure S1). The porous structure is also confirmed by TEM image; nevertheless, a selected-area electron diffraction (SAED) pattern recorded on the crystal showed a diffraction pattern corresponding to single-crystal anatase along the [001] zone axis (Figure 2c). High-resolution TEM (HRTEM) images taken from the junction of the TiO₂ particles revealed that single-crystal lattices exhibit atomic planes of anatase (200) or (020) crystal faces with a lattice spacing of around 0.189 nm (Figure 2d). These results strongly suggest the formation of Meso-TiO₂-500 with the {001} facet exposed.¹⁷ In addition, uniform lattice fringes are clearly observed across the image, confirming the perfectly oriented aggregation of TiO₂ nanocrystals. Owing to the

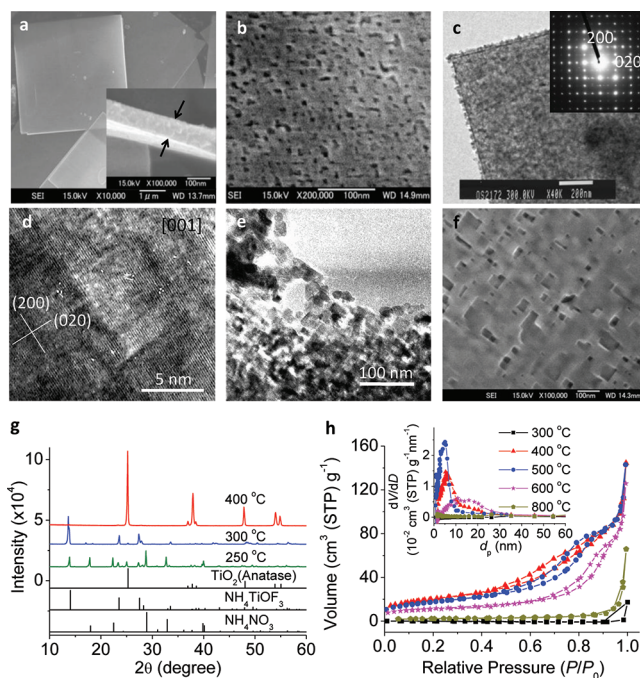


Figure 2. (a) SEM image of Meso-TiO₂-500 showing a plate-like morphology. (b) Magnified SEM image of a crystal surface revealing porous structures. (c) TEM image of a representative crystal showing a mesoporous structure, and SAED pattern (inset) showing single-crystal diffraction along the anatase [001] zone axis. (d) HRTEM image of the junction of several TiO₂ nanocrystals showing highly ordered lattices recorded from [001] orientation. (e) TEM image of the defective area on the edge of a TiO₂ mesocrystal. (f) SEM image of Meso-TiO₂ annealed at 800 °C. (g) XRD patterns and (h) N₂ adsorption-desorption isotherms and pore size distribution (inset) of the products obtained at different annealing temperature.

alternating arrangement of the nanocrystals, many gaps or pores are formed on the surface. The TEM image of a defective area of the crystal edge indicates that the nanocrystals are arranged in a regular structure via oriented attachment (Figure 2e). According to the literature,¹⁸ the nanocrystals are mutually attracted by van der Waals forces. The percentage of the aligned TiO₂ nanocrystals in a sample was about 80%. Energy-dispersive X-ray spectroscopy (EDX) (Figure S2) and X-ray photoelectron spectroscopy (XPS) (Figure S3) spectra confirmed that the impurities (such as N or F) on the TiO₂ surface are almost entirely removed after annealing in oxygen atmosphere. The band gap of the samples calculated from the steady-state diffuse reflectance spectra was about 3.2 eV (Figure S4), supporting the observation that synthesized Meso-TiO₂ is pure TiO₂.

To understand the formation mechanism, we compared the SEM images (Figures S5–S7), X-ray diffraction (XRD) patterns (Figure S8), N₂ adsorption-desorption isotherms, and pore size distribution (Figure 2h) of the samples obtained at different synthesis temperatures. The NH₄TiO₃ growth started at 250 °C with a mixture NH₄TiO₃ and NH₄NO₃ during the evaporation of water and pure NH₄TiO₃ was observed at 300 °C with a plate-like structure (Figure 2g). NH₄NO₃ and NH₄F are mainly used to control the composition and structure of product (Figures S5 and S6). There was no pore structure on the surface, and its specific surface area was very low (about 0.4 m² g⁻¹) (Figure 2h and Table 1). Interestingly, the sample had porous structures after

Table 1. Structural Parameters of Meso-TiO₂ and Reference TiO₂ Samples

| sample ^a | surface area (m ² /g) ^b | pore size (nm) ^c | pore volume (cm ³ /g) ^c | particle size (nm) ^d |
|----------------------------|---|-----------------------------|---|---------------------------------|
| Meso-TiO ₂ -300 | 0.4 | n.d. | n.d. | 45 |
| Meso-TiO ₂ -400 | 74 | 5 | 0.15 | 33 |
| Meso-TiO ₂ -500 | 63 | 5 | 0.2 | 39 |
| Meso-TiO ₂ -600 | 40 | 15 | 0.13 | 42 |
| Meso-TiO ₂ -700 | 13 | 20 | 0.04 | 59 |
| Meso-TiO ₂ -800 | 8 | 26 | 0.03 | 60 |
| Nano-TiO ₂ | 41 | 18 | 0.3 | 25 |
| Micro-TiO ₂ | 2 | 30 | 0.009 | >1000 |
| P-25 ^e | 55 | 19 | 0.21 | 25 |

^aMeso-TiO₂ samples annealed at different temperatures, named as Meso-TiO₂-T (T = annealing temperature). ^bThe Brunauer–Emmett–Teller (BET) method was utilized to calculate the specific surface area. ^cPore volume and pore diameter distribution was derived from the adsorption isotherms by the Barrett–Joyner–Halenda (BJH) model. ^dAverage size of anatase TiO₂ nanocrystals estimated from the Scherrer equation. ^eReference 19.

annealing at 400 °C. The specific surface area increased to 74 m² g⁻¹, and the pore size was about 5 nm. Moreover, the sample phase transformed into anatase TiO₂ with no apparent change in morphology (Figure S7). Due to the similar position of Ti atoms in both crystal structures, NH₄TiOF₃ could lead to the topotactic transformation to anatase after the removal of N, H, and F atoms from the crystal lattice by a simple heating process.⁹ Undoubtedly, the particle would shrink, resulting in

the decrease of the particle size from 45 nm (NH₄TiOF₃) to 33 nm (TiO₂) (Table 1). This inevitably resulted in space between nanocrystals to create the porous structures in the TiO₂ crystal. Upon further increasing the calcination temperature, the morphology and crystalline phase of TiO₂ remained unchanged (Figures S7 and S8), while the fusion of TiO₂ nanocrystals led to the increase of the particle size, simultaneously with the decrease of the specific surface area and the increase of the pore size (Figure 2f and Table 1). When TiO₂ was synthesized via the same synthetic route as Meso-TiO₂ without additives (NH₄NO₃ and NH₄F), the resultant material did not have a single-crystalline structure (Figure S9).

To demonstrate the intricate relationship between structure and function, we investigated photoinduced charge transfer properties of mesocrystal superstructures by means of conductive atomic force microscopy (AFM) equipped with a UV light source (365 nm, Figure S10).^{20,21} Figure 3a shows a typical AFM image of Meso-TiO₂-500 on an indium tin oxide (ITO) electrode. Without UV irradiation, there was no measurable current response to the applied voltage at the marked point (Figure 3b). On the other hand, a significant photocurrent response was observed with UV irradiation.²² Current–voltage curves represent the asymmetric characteristics, reflecting different electron injection efficiencies from platinum and ITO into the TiO₂ layer. From the size and thickness dependence of the photocurrent, the thickness of Meso-TiO₂ was found to have a primary effect on photocurrent generation (Figure 3c). The photoconductivity was then calculated to be $(1.9 \pm 0.5) \times 10^{-2} \Omega^{-1} \text{ m}^{-1}$ in air, which is comparable to or greater than that ($5.3 \times 10^{-3} \Omega^{-1} \text{ m}^{-1}$) reported for the nanocrystalline anatase TiO₂ film.²³

Two typical reference samples were chosen to compare: Nano-TiO₂ and Meso-TiO₂ annealed at 700 °C (Meso-TiO₂-700). The Nano-TiO₂ is a nanometer-sized single crystal with

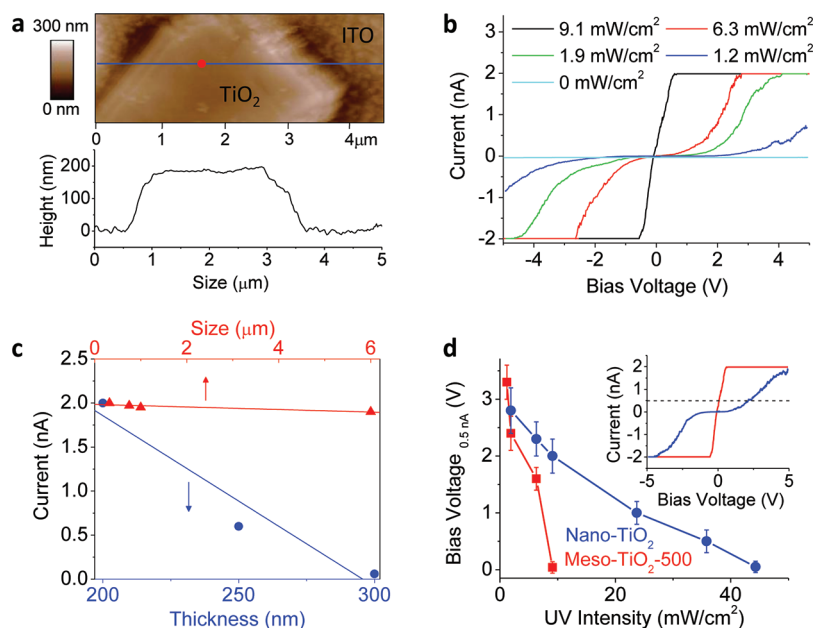


Figure 3. (a) (upper) AFM topological image of the Meso-TiO₂-500 immobilized on an ITO glass and (lower) cross-sectional profile along the blue line in the upper panel. The red dot indicates the location where current–voltage curves were measured. (b) Current–voltage curves measured for Meso-TiO₂-500 under 365-nm UV irradiation. (c) Size and thickness dependence on the photocurrent observed for Meso-TiO₂-500 at the same voltage and UV intensity (9.1 mW/cm²). The voltages applied for examining size and thickness dependence were +0.2 V and +1.0 V, respectively. (d) Response voltages achieving a current of 0.5 nA, plotted against UV intensity. The inset shows typical current–voltage curves measured for Meso-TiO₂-500 (red) and Nano-TiO₂ (blue) at constant UV intensity (9.1 mW/cm²).

truncated bipyramid morphology and a high surface area ($41 \text{ m}^2/\text{g}$) (Figure S11 and Table 1), which has anatase structure (Figure S12). The TEM analysis also revealed that the percentage of exposed $\{001\}$ facets of Nano-TiO₂ (43%) is similar to that of Meso-TiO₂ (38%). The inset of Figure 3d displays typical current–voltage curves measured for Meso-TiO₂-500 and aggregated Nano-TiO₂ under UV irradiation ($9.1 \text{ mW}/\text{cm}^2$), where regions of approximately the same thickness ($\sim 200 \text{ nm}$) were selected. More detailed results for Nano-TiO₂ and Meso-TiO₂-700 are given in Figures S14 and S15, respectively. The relationship between bias voltage and UV intensity needed to induce a current of 0.5 nA was examined to compare the photocurrent generation efficiencies of the samples (Figure 3d). Interestingly, the samples can be arranged in the decreasing order of photocurrent generation efficiency as follows: Meso-TiO₂-700, Meso-TiO₂-500, and Nano-TiO₂. The photocurrent attained its maximum at lower UV intensity in Meso-TiO₂ than it did in Nano-TiO₂, suggesting that electron transport ability is largely improved in Meso-TiO₂ possibly due to the intimate contact between nanocrystals (i.e., coherent particle–particle interface¹⁸) and between nanocrystals and electrodes (platinum AFM tip and ITO). Nevertheless, a sufficient number of lattice defects, such as vacancies, interstitials, and grain boundaries, still exist at the interface between adjacent nanocrystals in Meso-TiO₂-500. These defects should act as charge trapping sites that retard the charge transport across the mesoporous structure (Figure S16). After annealing at 700°C , the nanocrystals adhere to each other, thus reducing the number of trapping sites in Meso-TiO₂ and improving the photoconductivity.²⁴

To prove the enhanced performance of Meso-TiO₂, we examined the photocatalytic oxidation of *p*-chlorophenol (4-CP) and rhodamine B (RhB) and the photocatalytic reduction of Cr^{6+} in aqueous phase as probe reactions. Absorbance changes in characteristic absorption peaks were monitored to evaluate photocatalytic degradation activity (Figure S19). Here, three reference samples were chosen to compare the activity: Micro-TiO₂ (Figure S20), Nano-TiO₂, and commercial P-25 TiO₂ (Nippon Aerosil). The Micro-TiO₂ is a micrometer-sized single crystal with a truncated bipyramid morphology and a low specific surface area ($2 \text{ m}^2/\text{g}$). P-25 consists of anatase and rutile crystalline phases and is frequently used as a benchmark in photocatalysis.¹⁹

The results of the photocatalytic tests indicated that Meso-TiO₂-500 exhibits the highest activity in comparison to other samples annealed at temperatures ranging from 400 to 800°C (Figures 4a,b and S21). The photocatalytic activity increased by more than 30% with increasing calcination temperature from 400 to 500°C , because the porous structure of the sample became more ordered and the crystallinity improved. However, with further increase in the calcination temperature, the photocatalytic activity decreased drastically, mostly due to decrease in surface area (Table 1). Although there is much difference in the specific surface area between Meso-TiO₂-500 and Meso-TiO₂-700, the difference in the photocatalytic activity is relatively small. This discrepancy is partly due to the fact that the defect concentration in Meso-TiO₂ significantly decreased with increasing annealing temperature, which is conducive to the photocatalytic activity.²⁶

When photocatalytic activity of Meso-TiO₂ was compared with that of other reference samples, it was found that the Micro-TiO₂ sample showed the lowest photoactivity because it had the lowest specific surface area. Both the oxidation and

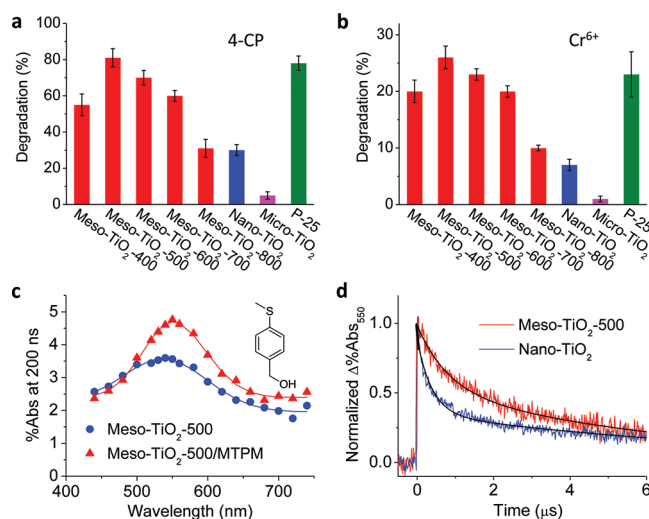


Figure 4. (a) Photocatalytic degradation of (a) 4-CP and (b) Cr^{6+} in aqueous phase in the presence of different TiO₂. (c) Time-resolved diffuse reflectance spectra observed at 200 ns after the laser flash during the 355-nm laser flash photolysis of Meso-TiO₂-500 in the absence and presence of MTPM (10 mM) in acetonitrile. The inset indicates the molecular structure of MTPM. The absorption peak at around 550 nm is assigned to MTPM^{•+}. (d) Differential time traces of %Abs at 550 nm obtained by subtracting the time trace observed in the absence of MTPM from that observed in the presence of MTPM (10 mM) for different TiO₂ samples in acetonitrile.

reduction photocatalytic activities of the Meso-TiO₂-500, Meso-TiO₂-600, and Meso-TiO₂-700 samples exhibited a 100–300% enhancement relative to that of Nano-TiO₂. Meso-TiO₂-600, and Nano-TiO₂ have similar surface area (Table 1); hence, the possibility that the observed dramatic activity enhancement is simply due to a difference in specific surface area can be excluded. The results also showed that Meso-TiO₂-500 had the highest photocatalytic activity, which was nearly similar to that of P-25 TiO₂.

Time-resolved diffuse reflectance spectroscopy was employed to measure the lifetime of a charge-separated state; this measure is a criterion for evaluating the efficiency of photocatalytic reactions.²⁷ As seen in Figure 4c, Meso-TiO₂-500 exhibits a broad transient absorption band in the visible to near-infrared range upon 355-nm laser excitation, which represents the overlapping of the trapped holes (mainly 440–600 nm) and trapped electrons (mainly 660–900 nm).²⁷ Herein, we selected 4-(methylthio)phenyl methanol (MTPM) as the probe molecule to estimate the lifetime of the charge-separated state (due to the specific spectroscopic properties of parent MTPM and the MTPM radical cation (MTPM^{•+}), which exhibits negligible absorption at the excitation wavelength for TiO₂ and absorption in the visible region (around 400–600 nm), respectively).²⁷ In fact, the addition of MTPM could make the transient signal more distinct (Figure 4c and S22). The absorption data of the 550-nm absorption band of MTPM^{•+}, which is generated by one-electron oxidation of adsorbed MTPM by the photogenerated holes,²⁷ can be used to determine the rate of charge recombination with the electrons in TiO₂. It should be noted that Meso-TiO₂-500 and Nano-TiO₂ showed similar adsorption equilibrium constants and total number of adsorption sites (Figure S23 and Table S1). Thus, Nano-TiO₂ is the best reference sample for eliminating the impact of adsorption on the reaction dynamics. As shown in Figures 4d and S24, the half-lives ($t_{1/2}$, the time required to

reach 50% of the initial % absorption (%Abs) values) of MTPM⁺ were determined to be $\sim 2 \mu\text{s}$ for the Meso-TiO₂ systems, which is much longer than that of Nano-TiO₂ ($\sim 0.5 \mu\text{s}$). Hence, Meso-TiO₂ could exhibit greatly increased photocatalytic activity due to its superstructure that enhances charge separation.

In summary, we have developed a facile approach for preparing anatase TiO₂ mesocrystal superstructures with high surface area and large {001} facet exposure. The highly enhanced photocatalytic activity of Meso-TiO₂ can be attributed to several factors: (1) the largely increased charge separation efficiency, which yields the long-lived reactive charges; (2) the large specific surface area, which provides abundant reaction sites for photocatalytic reactions; and (3) the highly efficient transportation of reactants and products owing to porous structure. Strategy and design principles described herein will open a new avenue for development of novel photoactive materials with potential applications in solar energy conversion and optoelectronic devices.

■ ASSOCIATED CONTENT

■ Supporting Information

Experimental and analytical procedures, and supporting table and figures. This material is available free of charge via the Internet at <http://pubs.acs.org>.

■ AUTHOR INFORMATION

Corresponding Author

*E-mail: tachi45@sanken.osaka-u.ac.jp (T.T.); majima@sanken.osaka-u.ac.jp (T.M.).

Notes

The authors declare no competing financial interest.

■ ACKNOWLEDGMENTS

The authors thank Prof. T. Kamegawa and Prof. H. Yamashita, Osaka University, for N₂ sorption measurements. T.M. thanks the World Class University program funded by the Ministry of Education, Science and Technology through the National Research Foundation of Korea (R31-2011-000-10035-0) for support. Z.B. thanks the JSPS for a Postdoctoral Fellowship for Foreign Researchers (No. P11041). This work has been partly supported by the Innovative Project for Advanced Instruments, Renovation Center of Instruments for Science Education and Technology, Osaka University, and a Grant-in-Aid for Scientific Research (Projects 22245022, and others) from the Ministry of Education, Culture, Sports, Science and Technology (MEXT) of the Japanese Government.

■ REFERENCES

- (1) Fujishima, A.; Zhang, X. T.; Tryk, D. A. TiO₂ Photocatalysis and Related Surface Phenomena. *Surf. Sci. Rep.* **2008**, *63*, 515–582.
- (2) Chen, X. B.; Shen, S. H.; Guo, L. J.; Mao, S. S. Semiconductor-Based Photocatalytic Hydrogen Generation. *Chem. Rev.* **2010**, *110*, 6503–6570.
- (3) Hagfeldt, A.; Boschloo, G.; Sun, L. C.; Kloo, L.; Pettersson, H. Dye-Sensitized Solar Cells. *Chem. Rev.* **2010**, *110*, 6595–6663.
- (4) Redl, F. X.; Cho, K. S.; Murray, C. B.; O'Brien, S. Three-Dimensional Binary Superlattices of Magnetic Nanocrystals and Semiconductor Quantum Dots. *Nature* **2003**, *423*, 968–971.
- (5) Kalsin, A. M.; Fialkowski, M.; Paszewski, M.; Smoukov, S. K.; Bishop, K. J. M.; Grzybowski, B. A. Electrostatic Self-assembly of Binary Nanoparticle Crystals with a Diamond-like Lattice. *Science* **2006**, *312*, 420–424.

- (6) Dong, A. G.; Chen, J.; Vora, P. M.; Kikkawa, J. M.; Murray, C. B. Binary Nanocrystal Superlattice Membranes Self-Assembled at the Liquid–Air Interface. *Nature* **2010**, *466*, 474–477.
- (7) Mann, S. Self-Assembly and Transformation of Hybrid Nano-objects and Nanostructures under Equilibrium and Non-equilibrium Conditions. *Nat. Mater.* **2009**, *8*, 781–792.
- (8) Cölfen, H.; Antonietti, M. Mesocrystals: Inorganic Superstructures Made by Highly Parallel Crystallization and Controlled Alignment. *Angew. Chem., Int. Ed.* **2005**, *44*, 5576–5591.
- (9) Zhou, L.; Smyth-Boyle, D.; O'Brien, P. A Facile Synthesis of Uniform NH₄TiOF₃ Mesocrystals and Their Conversion to TiO₂ Mesocrystals. *J. Am. Chem. Soc.* **2008**, *130*, 1309–1320.
- (10) Ye, J. F.; Liu, W.; Cai, J. G.; Chen, S. A.; Zhao, X. W.; Zhou, H. H.; Qi, L. M. Nanoporous Anatase TiO₂ Mesocrystals: Additive-Free Synthesis, Remarkable Crystalline-phase Stability, and Improved Lithium Insertion Behavior. *J. Am. Chem. Soc.* **2011**, *133*, 933–940.
- (11) Bian, Z. F.; Zhu, J. A.; Wen, J.; Cao, F. L.; Huo, Y. N.; Qian, X. F.; Cao, Y.; Shen, M. Q.; Li, H. X.; Lu, Y. F. Single-Crystal-like Titania Mesocages. *Angew. Chem., Int. Ed.* **2011**, *50*, 1105–1108.
- (12) Zhang, D. Q.; Li, G. S.; Wang, F.; Yu, J. C. Green Synthesis of a Self-Assembled Rutile Mesocrystalline Photocatalyst. *CrystEngComm* **2010**, *12*, 1759–1763.
- (13) Zhou, L.; O'Brien, P. Mesocrystals — Properties and Applications. *J. Phys. Chem. Lett.* **2012**, *3*, 620–628.
- (14) Lakshminarasimhan, N.; Kim, W.; Choi, W. Effect of the Agglomerated State on the Photocatalytic Hydrogen Production with in Situ Agglomeration of Colloidal TiO₂ Nanoparticles. *J. Phys. Chem. C* **2008**, *112*, 20451–20457.
- (15) Ismail, A. A.; Bahnmann, D. W. Mesosstructured Pt/TiO₂ Nanocomposites as Highly Active Photocatalysts for the Photo-oxidation of Dichloroacetic Acid. *J. Phys. Chem. C* **2011**, *115*, 5784–5791.
- (16) Gonzalez-Vazquez, J. P.; Morales-Flórez, V.; Anta, J. A. How Important is Working with an Ordered Electrode to Improve the Charge Collection Efficiency in Nanostructured Solar Cells? *J. Phys. Chem. Lett.* **2012**, *3*, 386–393.
- (17) Yang, H. G.; Sun, C. H.; Qiao, S. Z.; Zou, J.; Liu, G.; Smith, S. C.; Cheng, H. M.; Lu, G. Q. Anatase TiO₂ Single Crystals with a Large Percentage of Reactive Facets. *Nature* **2008**, *453*, 638–641.
- (18) Niederberger, M.; Cölfen, H. Oriented Attachment and Mesocrystals: Non-classical Crystallization Mechanisms Based on Nanoparticle Assembly. *Phys. Chem. Chem. Phys.* **2006**, *8*, 3271–3287.
- (19) Zhu, J.; Yang, J.; Bian, Z.-F.; Ren, J.; Liu, Y.-M.; Cao, Y.; Li, H.-X.; He, H.-Y.; Fan, K.-N. Nanocrystalline Anatase TiO₂ Photocatalysts Prepared via a Facile Low Temperature Nonhydrolytic Sol–Gel Reaction of TiCl₄ and Benzyl Alcohol. *Appl. Catal. B: Environ.* **2007**, *76*, 82–91.
- (20) Wang, S. J.; Zhang, X. T.; Cheng, G.; Jiang, X. H.; Li, Y. C.; Huang, Y. B.; Du, Z. L. Study on Electronic Transport Properties of WO₃/TiO₂ Nanocrystalline Thin Films by Photoassisted Conductive Atomic Force Microscopy. *Chem. Phys. Lett.* **2005**, *405*, 63–67.
- (21) Groves, C.; Reid, O. G.; Ginger, D. S. Heterogeneity in Polymer Solar Cells: Local Morphology and Performance in Organic Photovoltaics Studied with Scanning Probe Microscopy. *Acc. Chem. Res.* **2010**, *43*, 612–620.
- (22) Although Meso-TiO₂-500-Air, which is the sample annealed in air atmosphere, had a small amount of adsorbed F species on the TiO₂ surface (Figure S3c), it has little or no effect on the photoconductive properties (Figure S13).
- (23) Pomoni, K.; Vomvas, A.; Trapalis, C. Transient Photoconductivity of Nanocrystalline TiO₂ Sol–Gel Thin Films. *Thin Solid Films* **2005**, *479*, 160–165.
- (24) After switching off the UV light, Meso-TiO₂-500 had much longer photocurrent decay (more than 20 min) than did Meso-TiO₂-700 (about 1 min) and Nano-TiO₂ (about 5 min) (Figure S17). Since the photocurrent decay is attributed mainly to the scavenging of trapped electrons by oxygen molecules adsorbed on the surface (Figure S18),²⁵ the fast photocurrent decay observed for Meso-TiO₂-

700 would be due to a few interstitial trapping sites and the improved charge mobility.

(25) Tachikawa, T.; Majima, T. Exploring the Spatial Distribution and Transport Behavior of Charge Carriers in a Single Titania Nanowire. *J. Am. Chem. Soc.* **2009**, *131*, 8485–8495.

(26) Kong, M.; Li, Y.; Chen, X.; Tian, T.; Fang, P.; Zheng, F.; Zhao, X. Tuning the Relative Concentration Ratio of Bulk Defects to Surface Defects in TiO₂ Nanocrystals Leads to High Photocatalytic Efficiency. *J. Am. Chem. Soc.* **2011**, *133*, 16414–16417.

(27) Tachikawa, T.; Fujitsuka, M.; Majima, T. Mechanistic Insight into the TiO₂ Photocatalytic Reactions: Design of New Photocatalysts. *J. Phys. Chem. C* **2007**, *111*, 5259–5275.